Journal of
MATERIALS RESEARCH

Nondestructive evaluation of cavitation in an Al–Mg material deformed under creep conditions

Eric M. Taleff
Texas Materials Institute, University of Texas at Austin, Austin, Texas 78712

Teodoro Leon-Salamanca
Reinhart and Associates, Inc., Suite 173, P.O. Box 9802, Austin, Texas 78766

Richard A. Ketcham
Department of Geological Sciences, University of Texas at Austin, Austin, Texas 78712

Reuben Reyes
Aerospace Engineering Learning Resource Center, University of Texas at Austin, Austin, Texas 78712

William D. Carlson
Texas Materials Institute and Department of Geological Sciences, University of Texas at Austin,
Austin, Texas 78712

(Received 30 April 1999; accepted 20 October 1999)

Cavitation was examined in an Al–Mg solid-solution alloy deformed in tension at 400 °C under conditions providing solute-drag creep, which can produce tensile ductilities from 100% to over 300%. Two nondestructive evaluation techniques were employed to measure the extent of cavitation: ultra-high-resolution x-ray computed tomography and pulse-echo ultrasonic evaluation. Subsequent to nondestructive evaluation, the sample was sectioned for examination by standard metallographic techniques. Metallographic examination confirmed that both nondestructive techniques accurately indicated the extent of cavitation. Ultrasonic testing provided a practical means of distinguishing material with cavities from that without cavities. Ultra-high-resolution x-ray computed tomography provided an accurate three-dimensional image of internal cavitation.

I. INTRODUCTION

Recent investigations have revealed enhanced tensile ductility in Al–Mg solid-solution alloys deformed at warm and hot-working temperatures.[1–3] Enhanced ductility occurred during solute-drag creep associated with Mg solute additions in Al.[1–3] Under conditions promoting solute-drag creep, tensile ductilities of up to 325% have been observed in binary Al–Mg materials; this maximum value was achieved in an Al–2.8Mg (wt%) alloy at a temperature of 400 °C and a strain rate of 10^{-4} s^{-1}.[2] The large tensile ductilities observed in Al–Mg materials approach those of superplastic materials, yet do not require the fine grain sizes necessary to achieve superplasticity.[3] Thus, enhanced ductility in Al–Mg materials may be attractive where superplastic forming is not currently economical because of material costs. One of the important factors limiting tensile ductility during solute-drag creep of Al–Mg materials with ternary alloying additions, such as is typical of commercial 5xxx-series alloys, is cavitation.[2] It is this importance of cavitation in limiting enhanced ductility that prompted the present investigation. The goals of this investigation were (i) use nondestructive evaluation (NDE) techniques to measure the amount of cavitation in an aluminum alloy deformed under conditions promoting solute-drag creep, and (ii) correlate measurements of cavitation by NDE techniques with data from metallographic examination.

Cavitation was studied in a sample of ternary Al–Mg–Mn alloy deformed in tension at 400 °C under repeated step changes in strain rate until failure by cavity coalescence and ductile fracture. In addition to metallographic examination of the sectioned sample, two NDE techniques were utilized: ultra-high-resolution (UHR) x-ray computed tomography (CT) and pulse-echo ultrasonic evaluation. UHR x-ray CT scans provided two-dimensional images of the deformed sample's cross-section and a composite, three-dimensional image of its interior. This is the first report of UHR x-ray CT being used for such an application in a metal object.[4–6] Pulse-echo ultrasonic measurements were taken at three points along the gage region of the deformed sample. These data, when compared with data from undeformed material, indicated the extent of cavitation in the sample.

II. EXPERIMENTAL PROCEDURE

The composition of the aluminum sample studied is provided in Table I. The sample was tested at 400 °C in tension under repeated steps of constant true-strain rate, calculated based on the assumptions of constant volume and no neck formation.[1,2] An initial prestrain of approximately 20% elongation was introduced to stabilize the microstructure prior to stepping in strain rate. The range of strain rates varied from a low value of 10^{-4} s^{-1} at the first step to a high value of 2×10^{-2} s^{-1} at the last step of each series, with seven intermediate steps making a total of nine steps per series. Failure occurred during the seventh step of the third series repetition, at a true strain of 0.90 (145% elongation). Data from this test have been previously reported in the literature, and clearly indicate deformation controlled by solute-drag creep.[1,2] The primary factor limiting tensile ductility in this material under the prescribed conditions was cavitation.[1–3,7–10]

A. Metallography

A segment from the longest piece of the failed sample was subjected to UHR x-ray CT and pulse-echo ultrasonic evaluation prior to sectioning for metallography; the procedures for these NDE techniques will be presented subsequently. Width and thickness were measured with Vernier calipers at 2.5-mm increments along the length of both pieces of the failed sample for calculation of cross-sectional area reduction. After obtaining data from nondestructive evaluation, the entire sample was sectioned along its length. The longest piece of the failed sample was then cut into three separate segments for mounting in 32-mm-diameter molds for metallographic preparation. The mounted samples were ground and polished using standard metallographic preparation techniques. Measurements of cavity vol% were made at several positions using the point-count technique after polishing and prior to etching.[11] Measurements were made at a magnification of 32× using a grid-point spacing of 2.5 mm. After measuring cavity vol%, metallographic etching was performed using Barker's reagent and an electrolytic technique. Microstructures were then observed using an optical microscope with polarizing filters.

B. Ultrasonic evaluation

Ultrasonic evaluation was conducted prior to sectioning using a pulse-echo technique with a shear-wave transducer. The ultrasonic search unit had a central frequency of 15 MHz and a physical diameter of 5.4 mm. The width of the contact surface between the search unit and the sample was 2.3 mm. The sender provided a pulsed ultrasonic signal, and a fast digitizing computer board operating at 100 MHz acquired data from echoes of the original signal. Data for signal amplitude were obtained in both the time and frequency domains. Ultrasonic evaluation was conducted in an undeformed sample and at three positions on the longest piece of the failed sample: 13, 6, and 3 mm from the failure surface.

TABLE I. Alloy composition in wt%.

Al	Mg	Mn	Si	Fe	Cu	Zn	Ti
Balance	4.05	0.46	0.039	0.023	0.002	0.024	0.001

C. X-ray CT

UHR x-ray CT involved scanning planar sections of the failed sample's longest piece, perpendicular to its tensile axis. X-rays were produced using a microfocal source with a spot size of approximately 20 μm, operated at 150 kV and 0.153 mA. The detector system consisted of a 229-mm image intensifier and a charge-coupled device video camera system. Each scan field had a diameter of 4.7 mm and contained 3600 views with five samples per view. Each sample used 1/30 s of data acquisition. Each scan had a thickness of 30 μm and an offset between contiguous slices of 25 μm, providing 5 μm of overlap for each pair of contiguous slices. Data were taken by scanning three alternating slices simultaneously, requiring two passes of interleaved scans to acquire data in a continuous region. A region containing 36 contiguous slices was scanned using this method. This region extended from 1.2 to 2.1 mm below the failure surface. An additional 30-μm-thick scan slice was taken at 3.3 mm below the failure surface. Each data scan was digitized and saved in both 12- and 8-bit formats. The 12-bit data files were used for all analysis.

III. RESULTS

A. Metallography

The longest piece of the failed sample is shown at the top of Fig. 1 in a digital radiograph. Measurements of the cross-sectional area at several positions along the sample length were used to calculate true strain from area reduction, and these data are plotted against position in Fig. 1. The data indicate a significant rise in strain near the failure surface, as expected from necking. A composite micrograph of the sample interior near the failure surface is shown in Fig. 2 after being sectioned and polished. Measurements of cavity vol% were made from a similar composite micrograph at a magnification of 32×, taken before electrolytic etching. These data for cavity vol% are shown in the lower portion of Fig. 1, with the horizontal axis corresponding to distance along the digital radiograph.

Metallographic measurements of cavity vol% were compiled from both pieces of the failed sample and are plotted in Fig. 3 against true strain, measured from cross-sectional area reduction. True strain was computed with the constant-volume assumption, which neglects the effects of cavitation. True strain was not compensated for the effects of cavitation in order that direct comparisons to data in the literature can be made. These data indicate the expected exponential increase of cavity vol% with true strain. The data from Fig. 3 were evaluated on the basis of the following equation:[12]

$$C_V = C_{V_0} \exp\left(\eta(\epsilon - \epsilon_0)\right) \quad , \qquad (1)$$

in which C_V is cavity vol%, C_{V_0} is the concentration of cavities at a reference strain of ϵ_0, and η is the cavity growth rate. In fitting Eq. (1) to the data of Fig. 3, the reference strain was fixed at $\epsilon_0 = 0.25$. A least-squares fit resulted in the following relation:

$$C_V = 0.36 \exp\left(2.81(\epsilon - 0.25)\right) \quad . \qquad (2)$$

This fit to the data has a root-mean-square deviation of rmsd = 1.66. The cavity growth rate of $\eta = 2.81$ is higher than that typically found in superplastic materials, such as superplastic microduplex stainless steels, which have a cavity growth rate of approximately two.[10,13]

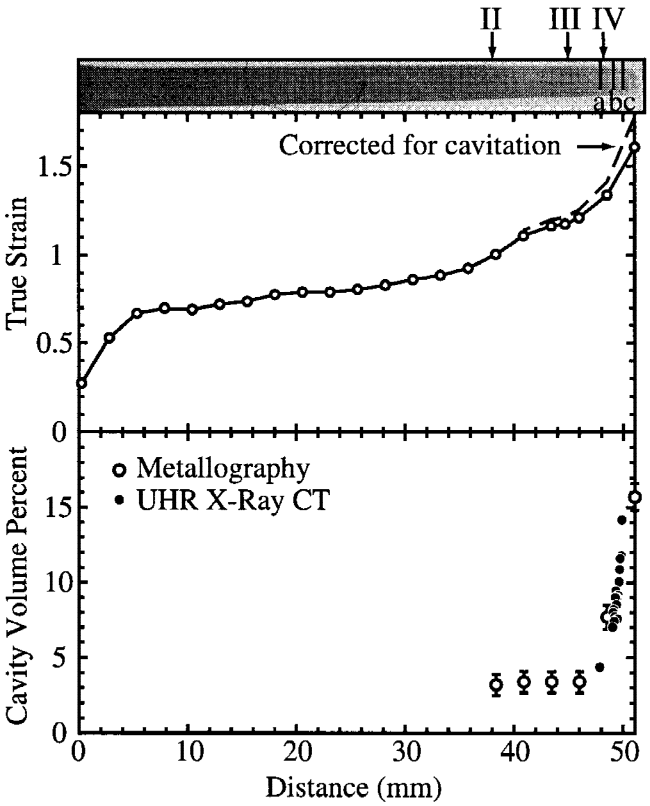

FIG. 1. A digital radiograph image is presented above plots of true strain and cavity content versus position. Ultrasonic measurements were made at positions labeled II, III, and IV on the radiograph image. UHR x-ray CT data were taken at position a and from positions b to c, as labeled on the radiograph image.

B. Ultrasonic evaluation

The results of pulse-echo ultrasonic evaluation are presented in Fig. 4 as plots of relative (unitless) amplitude against time and against frequency. Amplitude as a function of time is shown as dark traces plotted against the top axis, and amplitude as a function of frequency is shown as light traces plotted against the bottom axis. Frequency data are from analysis of the first "back wall" (BW) echo produced at each position using a fast Fourier transform (FFT) method; i.e., the BW signal was gated for analysis. Each graph of amplitude versus frequency was scaled such that the maximum amplitude of the BW echo reached full scale. Because of this scaling, the amplitudes of the frequency responses cannot be compared between the four different graphs of Fig. 4. Data were taken from an undeformed sample, graph I at the top of Fig. 4, and three positions within the gage region of the deformed sample. These three positions were located by the distance, *d*, from the failure surface of the longest piece of the failed sample. The positions were $d = 13$ mm, $d = 6$ mm, and $d = 3$ mm, which are given as positions II, III, and IV, respectively, at the top of Fig. 1.

Consider data from the undeformed sample, given in graph I at the top of Fig. 4. The initial pulse, which may be considered as the response shown at label A in graph I, initiated two echoes. The echo shown at label B was the first BW echo from the back surface of the sample, and the echo shown at C was a second BW echo produced from the portion of echo B reflected by the front surface of the sample. The natural attenuation of the aluminum, without cavities, caused a decrease in amplitude

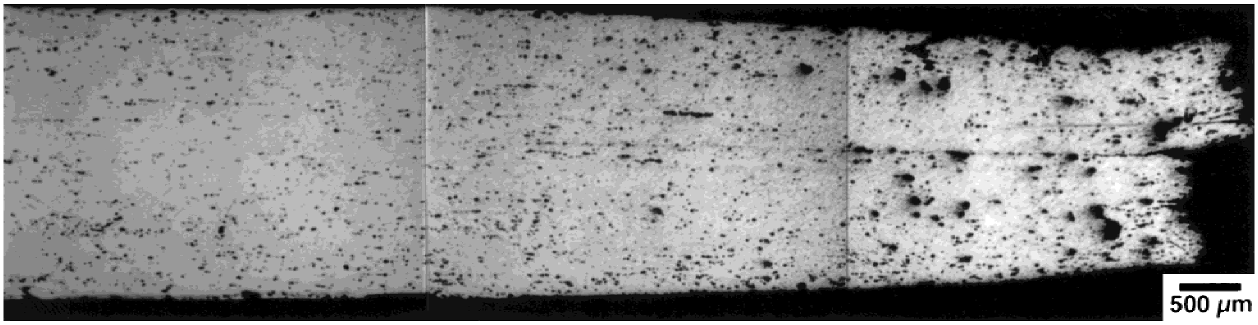

FIG. 2. This composite image from optical microscopy shows the interior of the long piece of the failed sample near the failure surface.

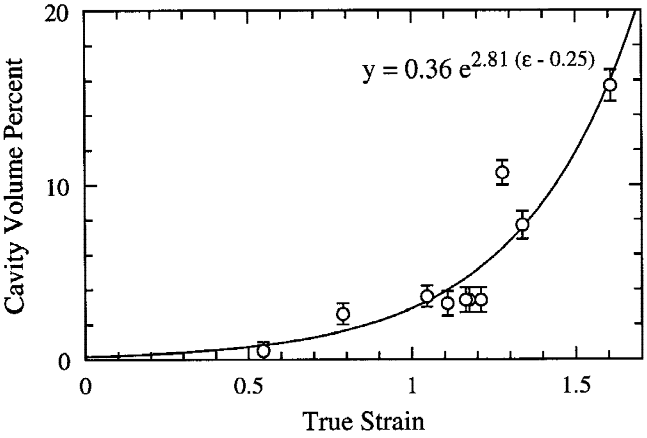

FIG. 3. Data from metallographic examination are plotted as cavity vol% against true strain measured from area reduction.

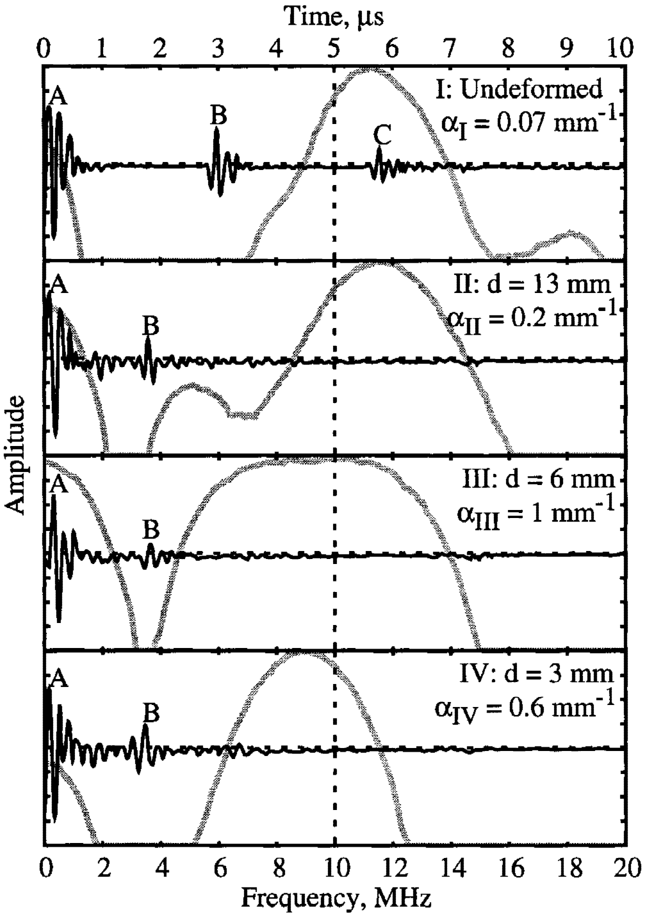

FIG. 4. Data from pulse-echo ultrasonic evaluation are presented as unitless amplitude against both time (dark traces measured against the top scale) and frequency (light traces measured against the bottom scale). Frequency data were taken by gating the signal from the first back wall echo, labeled as B in each graph. The four graphs represent I, an undeformed sample; II, a position 13 mm from the failure surface; III, a position 6 mm from the failure surface; and IV, a position 3 mm from the failure surface.

between echoes B and C. Natural attenuation significantly suppressed echoes beyond C. Data from the undeformed material indicated the time of travel across the sample thickness and back again, approximately 9.2 mm, was 2.8 μs. The shear wave velocity was calculated from these data to be 3300 m/s, approximately 6% higher than the value of 3100 m/s typically reported in the literature.[14] Measurements of signal velocity were not attempted in the deformed sections. The central frequency of the BW echo in the undeformed material was 11.2 MHz, which was a 25% decrease from the initial pulse. The logarithmic decrement in the signal was measured to be $\delta_I = 0.67$. The thickness of the undeformed sample was measured with calipers as $t_I = 4.6$ mm, giving an attenuation of $\alpha_I = 0.073\ \text{mm}^{-1}$ [$\alpha = \delta/(2t)$, where $2t$ is the distance traveled by the signal]. These data from the undeformed sample, as well as data from three positions on the longest piece of the failed sample, are reported in Table II. The general trend of increasing attenuation with increasing cavity concentration is observed, except at location IV (Fig. 1). One explanation for this is the dependence of attenuation on cavity sizes and frequency, which will be addressed in Sec. IV.

C. X-ray CT

Images from UHR x-ray CT scans of planar cross-sections in the deformed sample at the positions labeled a, b, and c in Fig. 1 are given in Fig. 5. These positions were 1.2, 2.1, and 3.3 mm below the failure surface, respectively. The images clearly indicate an increase in cavity concentration and typical cavity size near the failure surface. These images also indicate a reduction in cross-sectional area near the failure surface, as was measured by mechanical means (see Fig. 1).

All odd scan slices from positions a to b in Fig. 1 and the scan at position c were analyzed for cavity vol%. The 12-bit data were converted to 16-bit files and normalized by the CT values of air and aluminum. A cutoff CT value at 325/512 of full scale was used to distinguish pixels of data representing cavities, below the cutoff, from pixels of data representing aluminum, above the cutoff. The limitations of these procedures will be addressed in Sec.

TABLE II. Data from ultrasonic evaluation of an undeformed sample, location I, and three locations in the longest piece of the failed sample (II–IV) are provided as distance from the failure surface (d), sample thickness from measurement with calipers (t), logarithmic decrement (δ), attenuation (α), and cavity vol% from metallography (c).

Location	d (mm)	t (mm)	δ	α (mm^{-1})	c (%)
I	⋯	4.6	0.67	0.073	0.0
II	13	2.7	1.2	0.22	3.2
III	6	2.4	5.4	1.1	3.4
IV	3	2.3	2.7	0.59	7.7

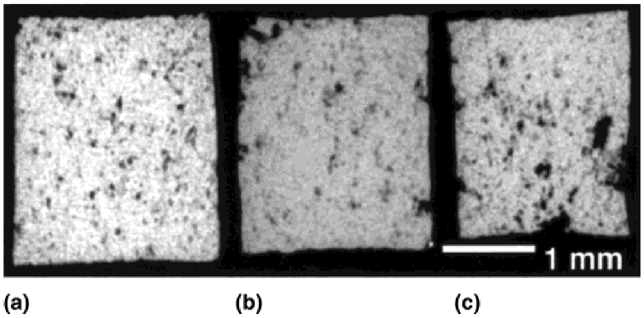

FIG. 5. (a–c) Three images from UHR x-ray CT data slices are presented. The images correspond to slices at positions a, b, and c, respectively, of Fig. 1.

IV. Identically sized boxes of data were taken within each slice for the computation of cavity vol%. The results from calculations of cavity vol% are presented in Fig. 1. Whereas the absolute value of cavity vol% depended strongly on the cutoff CT value chosen, the gradient in cavity vol% with position did not depend strongly on the cutoff CT value. The cutoff CT value was chosen to make the cavity vol% calculated from UHR x-ray CT data match that measured by metallography and remained the same at each position. The matching slopes of data in Fig. 1 from UHR x-ray CT and metallography confirm the choice of cutoff CT value and support the accuracy of UHR x-ray CT data in measuring cavity vol%.

Data from the 36 contiguous scan slices taken in section b–c, as labeled in Fig. 1, are presented in Fig. 6 as a three-dimensional reconstruction. The top image shows the aluminum material while the bottom image shows only the cavities. The bottom image is valuable in its representation of cavity geometry. Long cavities, which form by the interlinkage of several small cavities, are clearly evident along the tensile axis.

IV. DISCUSSION

A. Metallography

The micrographs in Fig. 7 clearly show cavity formation at grain boundaries and triple points, as indicated by arrows. The tensile axis is horizontal in Fig. 7, and is the direction in which cavities are elongated. The aluminum material in this investigation was previously found to contain fine particulates, most likely Al_6Mn proeutectic products.[1,2] Ternary aluminum alloys that contain particulates have been found to cavitate more readily than binary Al–Mg alloys without such particulates.[2] The particulates may act in conjunction with grain boundaries, with which they are often associated, as locations of cavity nucleation. Particulates can be present in stringers along the direction of rolling passes; the direction of rolling passes was the same as the tensile axis for the sample under investigation. Stringers can result in interconnected cavities along the direction of rolling passes, as suggested by the very long cavity indicated by the bottom arrow in Fig. 7(b).

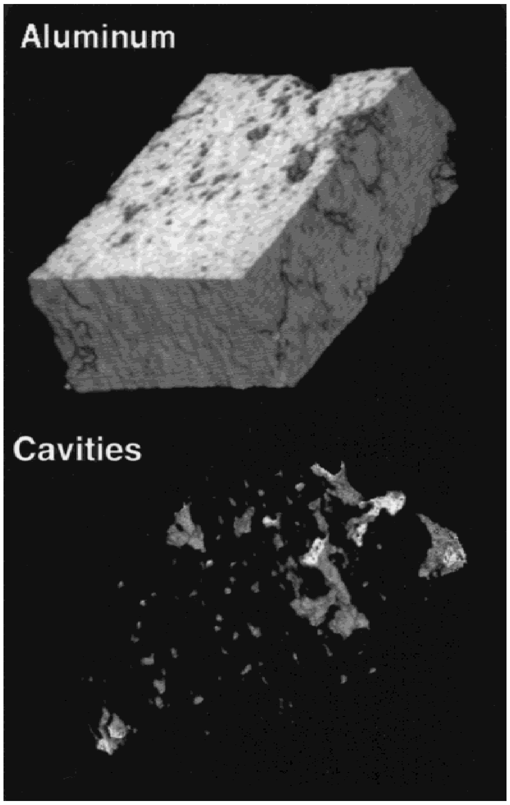

FIG. 6. Images of UHR x-ray CT data are shown indicating the aluminum material (top) and the cavities (bottom) between positions b and c indicated in Fig. 1.

B. Ultrasonic evaluation

Theoretical predictions of the expected ultrasonic response due to cavities in the aluminum sample can aid interpretation of data from ultrasonic evaluation. Attenuation by spherical cavities in an elastic medium is a function of cavity radius, number density, and the frequency of the ultrasonic signal.[15,16] Analytical results for the scattering cross section, γ, of longitudinal elastic waves by a single spherical cavity in an infinite medium are available from Ying and Truell.[15] Once γ has been calculated for a single cavity, the attenuation of multiple, noninteracting cavities is given by,[16,19]

$$\alpha = \tfrac{1}{2} n\gamma \quad , \tag{3}$$

where n is the number density of cavities. This attenuation can be rewritten in terms of the nondimensional function, Γ, following the work of Adler *et al.*,[16] which depends on the nondimensional quantity ka, where k is the magnitude of the wave vector and a is the cavity radius. This formulation is convenient for computational reasons, and yields the following relation:

$$\alpha = \pi a^2 n\Gamma \quad . \tag{4}$$

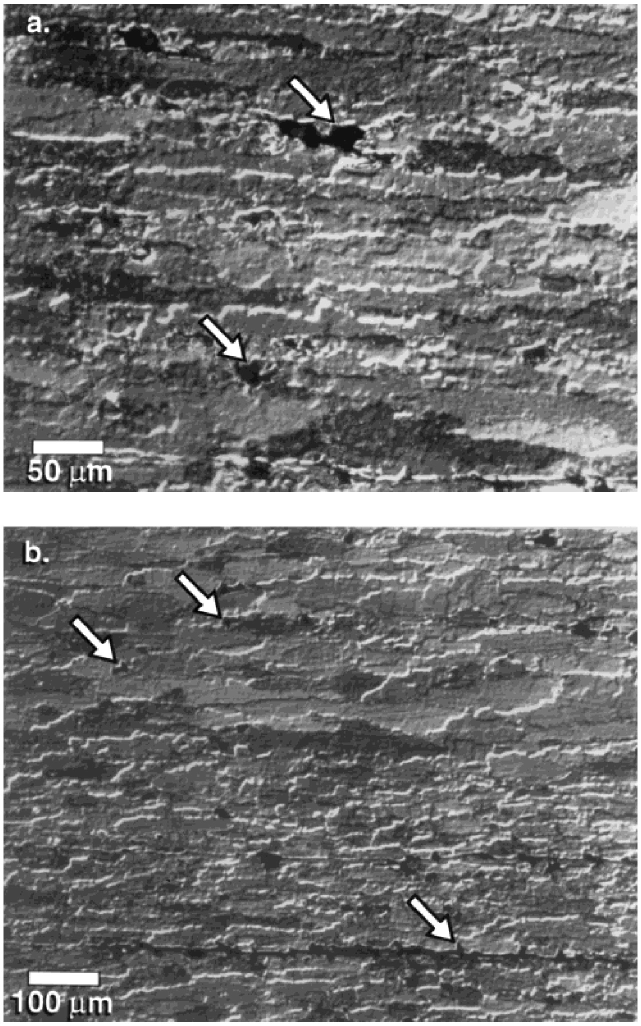

FIG. 7. (a,b) Optical micrographs are shown from the failed sample. The arrows indicate selected cavities.

Attenuation was calculated for cavitated aluminum in this manner as a function of frequency, cavity concentration, and cavity radius. These calculations predicted the relative attenuation at various frequencies for assumed cavity radii and number densities. These theoretical predictions were used to qualitatively predict the shapes of BW frequency responses, but not the logarithmic decrement in amplitude of the signal. These analytical models assume longitudinal elastic waves scattered by spherical, noninteracting cavities and do not allow the exact prediction of ultrasonic data obtained in this study, which used shear waves. These models, however, are extremely valuable when used to predict the general behaviors observed and determine the causes of these behaviors.

The amplitude of an input frequency spectrum is modeled by a function $I(f)$, where f is frequency. A normal distribution of frequency was assumed for the input spectrum, and its peak amplitude was scaled to a value of one. The central frequency of the input was assumed to be 11.2 MHz, and its standard deviation was taken as 2.5 MHz, as is plotted in Fig. 8. The amplitude of the BW frequency spectrum was then predicted for cavitated material using the following equation:

$$O(f) = I(f) \exp(-\alpha x) \quad , \tag{5}$$

where x is the distance traveled by the signal, assumed from the original sample thickness to be a constant value of 9.2 mm, an assumption that neglects sample thinning. The attenuation, α, was found from a sum of individually calculated attenuations when more than one cavity radius was assumed. For several different cavity sizes, each with attenuation α_i, total attenuation is given by

$$\alpha = \sum_i \alpha_i \quad . \tag{6}$$

The results of these calculations are presented in Fig. 9, which contains three plots of relative (unitless) amplitude versus frequency. The amplitude peak in each plot of Fig. 9 was scaled to unity, as were the data of Fig. 4.

The frequency response plotted in Fig. 9(a) assumed a cavity concentration of 6 vol% and a single cavity radius of 140 μm. A bimodal response was produced which closely resembles that of graph II (Fig. 4) in both shape and frequencies of the peaks in amplitude. This bimodal distribution was a direct result of a plateau in attenuation at high values of ka, as is demonstrated in Fig. 10 for four different cavity radii: 25, 50, 100, and 150 μm. A cavity concentration of 5 vol% was assumed for the values calculated in Fig. 10. The cavity size and density assumed to predict the bimodal response shown in Fig. 9(a) did not reproduce the volume fraction and diameters of cavities evident at location II in Fig. 1 because of previously discussed limitations in the analytical models used. These predictions do, however, explain the origin of the bimodal frequency response in Fig. 3, graph II.

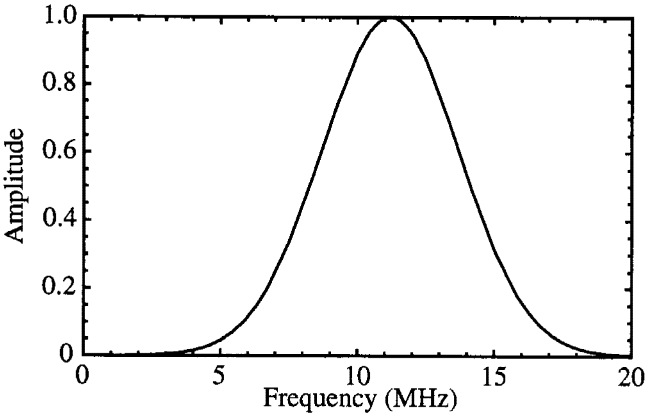

FIG. 8. The input signal used for theoretical predictions of frequency response is plotted as amplitude against frequency.

The plateau in attenuation versus frequency (Fig. 10) has another important ramification. The total attenuation predicted below 20 MHz in Fig. 10 for 5 vol% of cavities with a radius of 100 μm is greater than that for 5 vol% of cavities with a radius of 150 μm. This apparent contradiction of larger cavities providing less attenuation is a result of two effects: (i) a change in both the height and edge location of the plateau in attenuation with changing cavity radius, and (ii) a decrease in cavity number density with an increase in cavity radius at a constant cavity vol%. Herein lies an explanation for the ultrasonic data indicating $\alpha_{IV} < \alpha_{III}$, Fig. 4 and Table II, despite a higher cavity concentration at position IV than at III. A larger average cavity radius at position IV than at III could mimic the predictions in Fig. 10, leading to less attenuation at position IV. This result is most likely when an increase in average cavity radius shifts the attenuation plateau edge to a frequency equal to or less than that of the test signal, considered to be approximately 11.2 MHz in the present study.

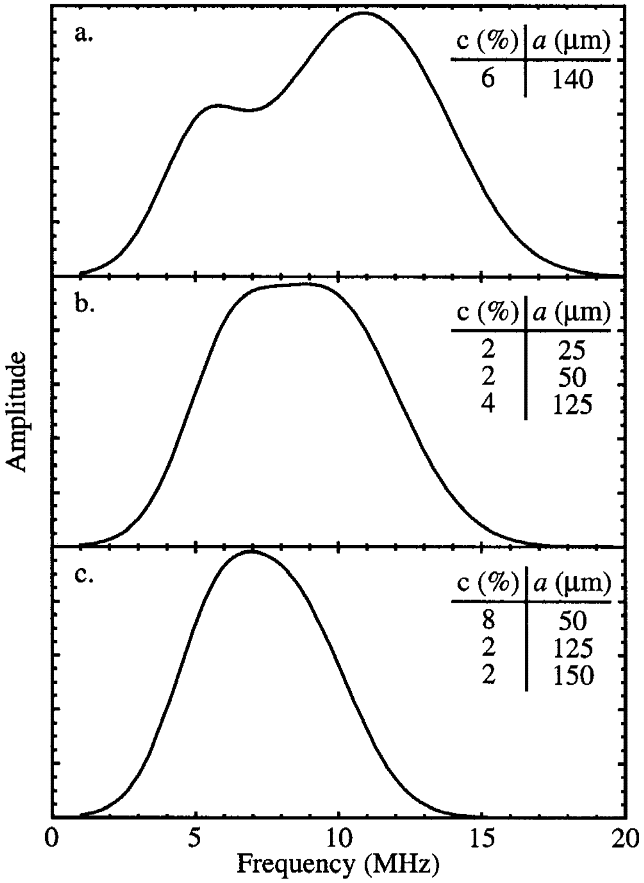

FIG. 9. (a–c) Three predicted frequency responses are plotted as unitless amplitude against frequency.

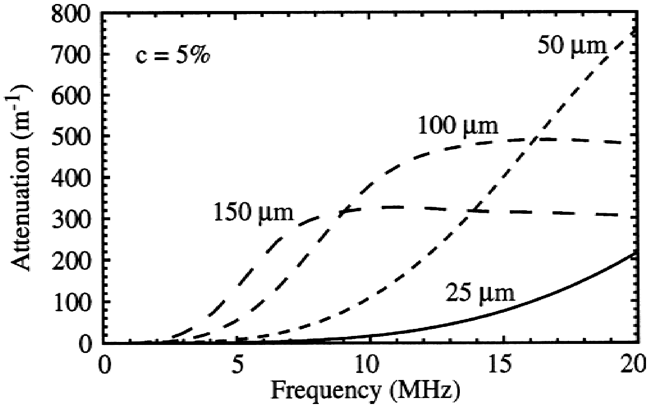

FIG. 10. Predictions of attenuation are plotted against frequency for four different cavity radii.

The BW response shown in Fig. 9(b) was produced by considering three different cavity sizes acting simultaneously. The cavity radii and concentrations assumed were 25 μm at 2 vol%, 50 μm at 2 vol%, and 125 μm at 4 vol%. The predicted response gave a plateau stretching over several MHz in frequency, which is quite similar to data in graph III of Fig. 4. The final BW response predicted is shown in Fig. 9(c), which assumed cavity radii and concentrations of 50 μm at 8 vol%, 125 μm at 2 vol%, and 150 μm at 2 vol%. Fig. 9(c) is similar to graph IV of Fig. 4.

These predictions based on analytical results were able to reproduce the shapes of BW frequency responses and provide explanations for these shapes. Experiments that measure cavity size and concentration have been conducted by Adler *et al.*, who used a wide spectrum of frequencies in order to measure the edge of the plateau in attenuation versus frequency.[16] Such measurements, although beyond the scope of the present investigation, provide very useful information on cavity size.[16] Practical application of ultrasonic evaluation to the determination of part quality degradation from cavitation may not require such advanced techniques. Graphs II through IV in Fig. 4 clearly indicate the presence of cavitation in the deformed material. In addition, differences in attenuation were clearly evident between undeformed material (Fig. 4, graph I), slightly cavitated material (Fig. 4, graph II), and extensively cavitated material (Fig. 4, graphs III and IV). Qualification of an industrial inspection process may require only the use of a few standard samples with and without cavitation to regularly calibrate the technique used in this investigation.

C. X-ray CT

A histogram of the UHR x-ray CT values at position c of Fig. 1 is presented in Fig. 11. The left peak represents data for air outside the sample volume. The right peak represents pixels of data corresponding to aluminum material with internal cavitation. It is noted that there is no peak in Fig. 11 that corresponds to the cavities within the sample volume. The primary reason for this is that the pixels that included cavities tended to also include some aluminum, and thus had CT values that reflected an av-

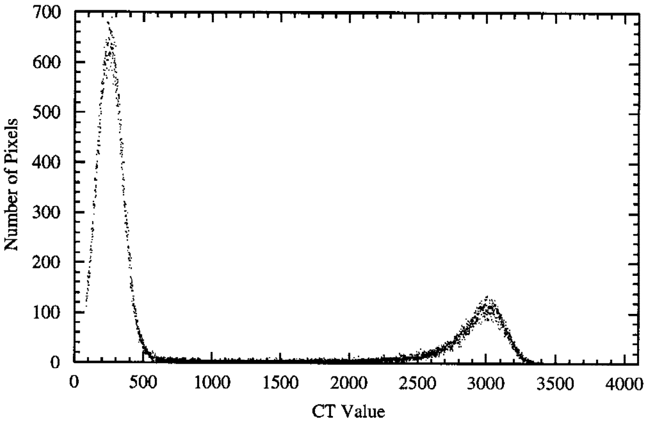

FIG. 11. A histogram of UHR x-ray CT data from a scan slice at position a of Fig. 1 is shown.

erage between the end-members of aluminum and air. This partial-volume effect was accentuated by slight blurring, attributed to the finite resolution of the data and the image reconstruction process, causing pixel values to be slightly contaminated by material from surrounding pixels. Because of these factors, data for cavities spanned the continuum from the left slope of the right peak in the histogram to the right slope of the left peak.

The approach to cavity vol% calculations employed here required calibration of a cutoff CT value, for which data from metallographic evaluation were used. A more independent and rigorous porosity calculation can also be used that explicitly takes partial-volume effects into account, but requires careful calibration of the CT values of the end-member materials, in this case nonporous aluminum and air. In the absence of such calibrations, the cutoff approach provided a good measure of cavity vol%. UHR x-ray CT provided measurements of cavity vol% in sections spaced much more closely than is easily accomplished using traditional metallographic methods.

UHR x-ray CT data are extremely valuable for visualizing cavity morphology. The interlinkage of cavities along the tensile axis, shown in Fig. 6, clearly demonstrates this. The ability of UHR x-ray CT to image cavity morphology is limited to the later stages of cavity growth because only cavities of approximately 25 μm and larger can be resolved accurately on the equipment employed for this investigation. The resolution of finer structures would require a CT system with a synchrotron, or similar x-ray source, often referred to as "micro-CT."[20–22] Alternatives to this are primarily destructive techniques, such as electron microscopy, which may be used for studying the morphology of cavities during nucleation and the initial stages of growth.

V. CONCLUSIONS

(1) Ultrasonic evaluation clearly differentiated between aluminum materials with no cavitation, slight cavitation, and extensive cavitation.

(2) Analytical predictions of frequency response from the scattering of noninteracting, spherical cavities in aluminum produced frequency response curves similar to those obtained by ultrasonic evaluation and explains the origins of their shapes.

(3) UHR x-ray CT data were used to image cavity morphology during the later stages of cavity growth and interlinkage, where structures were significantly larger than 25 μm.

(4) After calibration using accurate metallographic data for cavity vol%, UHR x-ray CT data were used to quantitatively measure cavity vol%.

ACKNOWLEDGMENTS

This work was supported by the National Science Foundation under Grant No. DMR-9702156. Additional support for this work was provided by Reinhart and Associates, Inc., Austin, Texas. UHR x-ray CT data and images were produced at the High-Resolution X-Ray Computed Tomography Facility of the University of Texas at Austin, supported by National Science Foundation Grant No. EAR-9816020. The authors thank Dr. Donald R. Lesuer of Lawrence Livermore National Laboratory for providing the aluminum sample. The lead author thanks Professor Mark Hamilton for useful discussions on the subject of scattering phenomena.

REFERENCES

1. E.M. Taleff, D.R. Lesuer, and J. Wadsworth, Metall. Mater. Trans. **27A,** 343 (1996).
2. E.M. Taleff, G.A. Henshall, T.G. Nieh, D.R. Lesuer, and J. Wadsworth, Metall. Mater. Trans. **29A,** 1081 (1998).
3. E.M. Taleff and P.J. Nevland, JOM **51,** 34 (1999).
4. R.A. Ketcham and W.D. Carlson, Computers and Geosciences (in press).
5. E.M. Withjack, SPE Formation Evaluation **3,** 696 (1988).
6. S.L. Wellington and H.J. Vinegar, J. Petrol. Technol. **39,** 885 (1987).
7. E.M. Taleff, G.A. Henshall, D.R. Lesuer, and T.G. Nieh, in *Aluminum Alloys: Their Physical Properties and Mechanical Properties (ICAA4)*, edited by T.H. Sanders and E.A. Starke, Jr. (Georgia Institute of Technology, Atlanta, GA, 1994), p. 338.
8. E.M. Taleff, G.A. Henshall, D.R. Lesuer, T.G. Nieh, and J. Wadsworth, in *Superplasticity and Superplastic Forming,* edited by A.K. Ghosh and T.R. Bieler (TMS, Warrendale, PA, 1995), p. 3.
9. E.M. Taleff, G.A. Henshall, D.R. Lesuer, T.G. Nieh, and J. Wadsworth, in *Aluminum and Magnesium for Automotive Applications,* edited by J.D. Bryant and D.R. White (TMS, Warrendale, PA, 1995), p. 125.
10. E.M. Taleff, D.R. Lesuer, C.K. Syn, and G.A. Henshall, in *Recent Advances in Fracture,* edited by R.K. Mahidhara, A.B. Geltmacher, P. Matic, and K. Sadananda (TMS, Warrendale, PA, 1997), p. 295.
11. *Metals Handbook, Desk Edition,* edited by H.E. Boyer and T.L. Gall (American Society for Metals, Metals Park, OH, 1985), p. 36·16.
12. S. Lian and M. Suery, *Mater. Sci. Technol.* **2,** 1093 (1986).

13. T.G. Nieh, D.R. Lesuer, and C.K. Syn, Mater. Sci. Eng. **A202,** 43 (1995).
14. M.A. Meyers, *Dynamic Behavior of Materials* (Wiley, New York, 1994), pp. 38, 42.
15. C.F. Ying and R. Truell, J. Appl. Phys. **27,** 1086 (1956).
16. L. Adler, J.H. Rose, and C. Mobley, J. Appl. Phys. **59,** 336 (1986).
17. L. Adler and S-W. Wang, in *Analytical Ultrasonics in Materials Research and Testing* (NASA Scientific and Technical Information Branch, Washington, DC, 1986), p. 75.
18. L. Adler, in *The Evaluation of Materials and Structures by Quantitative Ultrasonics: International Centre for Mechanical Sciences, Courses and Lectures–No. 330*, edited by J.D. Achenbach (Springer-Verlag, New York, 1993), p. 161.
19. J.E. Gubernatis and E. Domany, Wave Motion **6,** 579 (1984).
20. J.H. Kinney, T.M. Breuning, T.L. Starr, D. Haupt, M.C. Nichols, S.R. Stock, M.D. Butts, and R.A. Saroyan, Science **260,** 789 (1993).
21. B.P. Flannery, H.W. Deckman, W.G. Roberge, K.L. D'Amico. Science **237,** 1439 (1987).
22. D.A. Coker, S. Torquato, and J.H. Dunsmuir, J. Geophys. Res. **101,** 17497 (1996).